

# Self-supervised machine learning pushes the sensitivity limit in label-free detection of single proteins below 10 kDa

**Mahyar Dahmardeh**

Max Planck Institute for the Science of Light <https://orcid.org/0000-0001-8204-0652>

**Houman Mirzaalian Dastjerdi**

Max Planck Institute for the Science of Light

**Hisham Mazal**

Max Planck for the science of light <https://orcid.org/0000-0002-2071-9552>

**Harald Köstler**

Department of Computer Science, Friedrich-Alexander-Universität Erlangen-Nürnberg

**Vahid Sandoghdar** (✉ [vahid.sandoghdar@mpl.mpg.de](mailto:vahid.sandoghdar@mpl.mpg.de))

Max Planck Institute for the Science of Light <https://orcid.org/0000-0003-2594-4801>

---

## Article

### Keywords:

**Posted Date:** June 2nd, 2022

**DOI:** <https://doi.org/10.21203/rs.3.rs-1635524/v1>

**License:**   This work is licensed under a Creative Commons Attribution 4.0 International License.

[Read Full License](#)

---

# 1 Self-supervised machine learning pushes the 2 sensitivity limit in label-free detection of single 3 proteins below 10 kDa

4 Mahyar Dahmardeh<sup>1,2,†</sup>, Houman Mirzaalian Dastjerdi<sup>1,2,3,†</sup>, Hisham Mazal<sup>1,2</sup>, Harald  
5 Köstler<sup>3,4</sup>, and Vahid Sandoghdar<sup>1,2,5,\*</sup>

6 <sup>1</sup>Max Planck Institute for the Science of Light, 91058 Erlangen, Germany.

7 <sup>2</sup>Max-Planck-Zentrum für Physik und Medizin, 91058 Erlangen, Germany.

8 <sup>3</sup>Department of Computer Science, Friedrich-Alexander-Universität Erlangen-Nürnberg, 91058 Erlangen, Germany.

9 <sup>4</sup>Erlangen National High Performance Computing Center (NHR@FAU).

10 <sup>5</sup>Department of Physics, Friedrich-Alexander-Universität Erlangen-Nürnberg, 91058 Erlangen, Germany.

11 \*To whom correspondence should be addressed. E-mail: vahid.sandoghdar@mpl.mpg.de

12 †these authors contributed equally to this work

## 13 ABSTRACT

14 Interferometric scattering (iSCAT) microscopy is a label-free optical method capable of detecting single proteins, localizing their binding positions with nanometer precision, and measuring their mass. In the ideal case, iSCAT is limited by shot noise so that collection of more photons should allow its detection sensitivity to biomolecules of arbitrarily low mass. However, a number of technical noise sources combined with speckle-like background fluctuations have restricted the detection limit in iSCAT. Here, we show that an unsupervised machine learning isolation forest algorithm for anomaly detection pushes the mass sensitivity limit by a factor of four to below 10 kDa. We implement this scheme both with a user-defined feature matrix and a self-supervised FastDVDNet and validate our results with correlative fluorescence images recorded in total internal reflection mode. Our work opens the door to the optical detection of small traces of disease markers such as alpha-synuclein, chemokines, and cytokines.

15 Analysis of nanometer-scale matter is of utmost importance for a variety of biomedical investigations<sup>1-5</sup>. Over the period of  
16 about one century, many clever techniques have been invented for characterization of macromolecules, e.g., to resolve structure,  
17 map dynamics, assess chemical composition, and measure physical quantities such as size and weight. Methods based on  
18 nuclear magnetic resonance spectroscopy, electrophoresis, mass spectrometry, electron microscopy, fluorescence imaging, and  
19 plasmon resonance spectroscopy have introduced decisive advantages, but each approach also confronts limitations. Thus, new  
20 innovations are continuously sought to push the measurement boundaries. Optical methods are desirable in this quest because  
21 they can be non-invasive and compatible with real-time studies. Indeed, the optical cross section of matter is intrinsically large,  
22 making it possible to detect single molecules and proteins in direct extinction measurements<sup>6-8</sup>, where the incident field (or a  
23 fraction of it) interferes with the tiny amount of light that is coherently scattered by the nano-object of interest<sup>9-11</sup>.

24 The interferometric signal that is generated by the scattered light (iSCAT) not only allows one to detect and sense sub-  
25 wavelength nanoparticles such as single proteins, but it also reports on the particle size<sup>8</sup>. Indeed, iSCAT measurements have  
26 recently been calibrated to determine protein mass<sup>11,12</sup>, leading to a technology that is now also offered as a commercial  
27 solution (Refeyn Ltd). Since the sensitivity of iSCAT is ultimately limited by shot noise<sup>10,13,14</sup>, one could expect to detect an  
28 arbitrarily small amount of matter if only one could collect a sufficiently large number of photons. In practice, however, the  
29 performance falls short of this ideal situation<sup>14</sup> so that proteins lighter than about 40 kDa have not been detected<sup>11</sup>. In this work,  
30 we report on a substantial improvement in iSCAT detection sensitivity to the range of 9 kDa. In addition to implementing a  
31 robust optical setup, the key enabling technology that provides this sensitivity is the use of machine learning approaches in  
32 “anomaly detection”<sup>15</sup>. We benchmark and validate our results by performing fluorescence detection in total internal reflection  
33 (TIRF) mode.

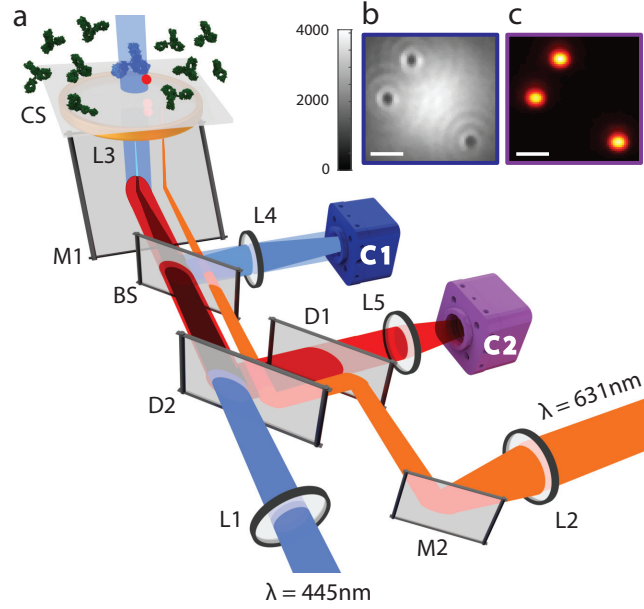
## 34 The iSCAT signal

Fig. 1a shows the iSCAT sensing setup. A laser beam centered at a wavelength of  $\lambda = 445$  nm illuminates a sample that consists of an aqueous buffer on a microscope coverglass. A fraction of the incident light is reflected at this interface and is utilized as

reference in its interference with the scattered light from the nano-object under study<sup>10,13</sup>. The detected optical power on the camera reads

$$P_d \propto |E_r|^2 + |E_s|^2 + 2|E_r||E_s|\cos\phi, \quad (1)$$

where  $E_i$ ,  $E_r = rE_i$ , and  $E_s = sE_i$  denote the electric fields of the incident, reference, and scattered light fields, respectively, and  $\phi$  signifies the phase difference between the latter two quantities. To add fluorescence imaging capabilities, a laser beam at  $\lambda = 631$  nm is used to illuminate the sample in TIRF mode through the same microscope objective. The fluorescence signal is filtered through a dichroic mirror and is imaged on a second camera. Fig. 1b shows an example of the iSCAT image for 100 nm polymer beads bound to the coverglass. In Fig. 1c, we depict the TIRF image of the same beads, which contained fluorescent dyes.



**Fig. 1.** **a**, Sketch of the optical setup. A laser beam at  $\lambda = 445$  nm is focused at the back focal plane of an oil-immersion objective to generate a quasi-collimated beam with a diameter of ca.  $6 \mu\text{m}$  at the sample surface. The sample chamber consists of a microscope coverglass sealed to the bottom of a plexiglass dish containing 2 ml of buffer solution.  $L1$ ,  $L2$ ,  $L3$ ,  $L4$ , and  $L5$  denote lenses, including the microscope objective.  $CS$ ,  $BS$  and  $M1$  signify the coverglass, beam splitter and the objective coupling mirror, respectively.  $D1$ ,  $D2$  and  $M2$  show the dichroic filters and mirror used for guiding the TIRF beam.  $C1$ ,  $C2$  represent the iSCAT and TIRF imaging cameras. **b**, Experimental iSCAT image of 100 nm fluorescent beads deposited on the coverglass. **c**, TIRF image of the same beads as in **(b)**. Scale bars in **(b,c)** correspond to  $1.5 \mu\text{m}$ .

The scattered field of a nanoparticle is proportional to the incident field via its polarizability ( $\alpha$ ) so that  $s \propto \alpha$ . For small nano-objects, the intensity of the scattered light ( $|E_s|^2$ ) becomes negligible compared to the other terms in equation (1). Hence, it follows that the iSCAT contrast ( $C$ ) of a small particle can be formulated as,

$$C = \frac{P_d - P_r}{P_r} \sim 2 \frac{|E_s|}{|E_r|} \cos\phi = 2 \frac{s}{r} \cos\phi, \quad (2)$$

where  $P_d$  and  $P_r$  refer to the detected and reference powers, respectively. Considering that  $\alpha$  is proportional to the particle volume and assuming a constant density for protein matter, one can conclude that  $C$  is linearly proportional to the particle mass  $m$ <sup>8</sup>. Thus, the iSCAT signal provides a measure for mass photometry<sup>11,12</sup>.

The iSCAT image in Fig. 1b was recorded in one frame within a short exposure time of  $20 \mu\text{s}$ . Visualizing single proteins, however, requires longer integration times and an elaborate analysis to account for the speckle-like background features that are caused by coherent scattering from slight imperfections of the sample surface<sup>14</sup>. In a nutshell, this analysis exploits the temporal change of the signal as a protein lands on the sensor substrate to eliminate the static background of the sample by comparing each video frame with its neighbors. In practice, a series of careful steps establish an algorithm that performs a differential rolling average (DRA) of several hundred camera frames, followed by the application of various tools for the

53 identification of the footprint of individual proteins and for determining their iSCAT contrasts<sup>8,12</sup>. This procedure is presented  
54 in a recent publication<sup>14</sup> and is described in Section 3 of the Supplementary Information (SI).

## 55 Results

56 In Fig. 2a, we show an example of the raw image recorded on the iSCAT camera from a sample containing bovine serum  
57 albumin (BSA, molecular mass of 66 kDa). Fig. 2b discloses the foot print of a single protein from that measurement after a  
58 typical DRA analysis on 1500 neighboring frames. While succeeding in the detection of a small protein, the image also reveals  
59 background fluctuations that are not fully eliminated by the existing algorithm, possibly due to various electronic, mechanical,  
60 or fluidic sources of noise (see Section 1 of SI and Ref. <sup>14</sup> for details).

61 For our current discussion, it suffices to consider the residual signal fluctuations as “noise” in the recognition of the particle  
62 contrast, which acts as the “signal”. Thus, the problem can be reduced to the challenge of deciphering image features at a  
63 given signal-to-noise ratio (SNR). In our setup, proteins with molecular mass of 40 kDa, which is the lowest that has been  
64 reported in the literature<sup>11</sup> yield  $\text{SNR} \sim 3$ , whereby the noise level is defined as the root mean square (RMS) of the residual  
65 background fluctuations. Here, it is important to note that the resulting noise is not white because the interference features of  
66 the background are governed by the same instrument response function that determines the system point spread function (PSF).  
67 This structured background makes it particularly difficult to identify the signal<sup>16</sup>. In this work, we show that application of  
68 machine learning algorithms allows us to detect proteins as small as 9 kDa, corresponding to  $\text{SNR} \sim 1.4$  in our setup.

69 To underpin our results, we labelled the proteins under study with ATTO647 dye molecules with a negligible molecular  
70 weight of about 0.7 kDa at a 1:1 labelling ratio and monitored them via the accompanying TIRF detection, as displayed in  
71 Fig. 2c. To check the purity of the protein samples after labeling, we ran a gel electrophoresis (SDS-PAGE) which can be found  
72 in SI (see section 2). We note that the iSCAT and TIRF measurements were interlaced with typical repetition cycles of 30 s in  
73 order to minimize bleaching and photoswitching of the fluorescence by the iSCAT illumination. This scheme also eliminated  
74 any spurious background in the iSCAT image that might stem from the fluorescence excitation laser.

## 75 Anomaly Detection

76 To push the detection sensitivity beyond the currently accessible level, we implemented anomaly detection (AD) based on  
77 isolation forest (iForest)<sup>17</sup>, which has been successfully applied to computer vision, signal processing, and communication  
78 applications<sup>15, 18–20</sup>. AD encompasses a general class of algorithms, where one first establishes a “normal” signal and then  
79 identifies deviations or “anomalies” that are caused by a dynamic event. The normal signal in our experiment is defined as the  
80 background image obtained by averaging over multiple frames right before and after the frames that contain the landing of a  
81 given protein. We present two approaches for distinguishing the normal and anomalous events in our analysis.

82 In the first approach, the user chooses a set of temporal statistical features (mean, standard deviation, etc.) and spatial  
83 features (e.g., PSF-like features that result from DRA) that are evaluated for a certain pixel range in each image frame (see SI,  
84 Figs. 3-4 for details). A given frame  $t$  is then re-shaped for each feature into a 1D vector with elements representing the pixel  
85 values of that frame. Next, a user-defined matrix is generated by putting together the 1D vectors from all selected features.  
86 The resulting “feature matrix” is classified by iForest, which is an unsupervised machine learning algorithm that applies a  
87 feature space transform based on a comparison with the neighboring frames and pixels. The output of iForest is a vector of true  
88 (anomalous) and false (normal) values for each pixel.

## 89 Benchmarking for a known sample

90 Fig. 2d presents the accumulation of the resulting anomalous pixels during a protein binding event for all frames that were used  
91 to detect the protein under discussion (see SI, Fig. 4c). To discriminate against false positive events, we apply a morphological  
92 operation, whereby unconnected anomalous pixels in each frame are eliminated. In the case of the data in Fig. 2d, the  
93 morphological operation considered anomalous pixels that were accompanied by at least one more neighboring pixel (see SI,  
94 Table 1). In a next step, the image in Fig. 2d is convolved with a Gaussian function that fits our experimental PSF, and a simple  
95 threshold is set to produce a binary mask for identifying hot regions (see Fig. 2e). A comparison with the conventional DRA  
96 and TIRF measurements (see Figs. 2b,c) reveals a very good agreement with the outcome of AD based on user-defined criteria.

97 The process of feature extraction in AD is decisive for the quality of the resulting classification. It is thus desirable to make  
98 it independent of the settings and criteria chosen by the user. To realize an autonomous feature extraction step, we implemented  
99 a tailor-made FastDVDNet<sup>21</sup> as a cutting-edge deep neural network (DNN). Here, a frame  $t$  is analyzed by comparing it with  
100 its neighboring frames  $t - k$  and  $t + k$ , where  $k$  is a suitable stride (see SI, Table 1). In this approach, the feature matrix is  
101 composed of the 1D vectors that result from the aforementioned frames (see SI, Fig. 5a). The outcome is again fed to iForest  
102 for classification.

103 Fig. 2f shows the result of AD based on DNN for the protein landing event of Fig. 2b. It can be seen that as opposed to  
104 the user-defined scenario presented in Fig. 2d, DNN can effectively isolate the entirety of a PSF in each frame, significantly

105 increasing the detection yield. We remark that to eliminate artifacts near the borders and corners of a frame, we only considered  
 106 the data within a circular mask of radius  $R = 33$  pixels. We find that in the case of a 66 kDa protein, both AD approaches  
 107 succeed to localize the protein with sub-pixel accuracy. The added value of DNN is manifested at low SNRs, where the user  
 108 fails to manually and visually detect the PSFs. More details on the performance of this method, its benchmarking against  
 109 experimental data, and on comparison with the user-defined feature matrix are given in SI (see section 6).

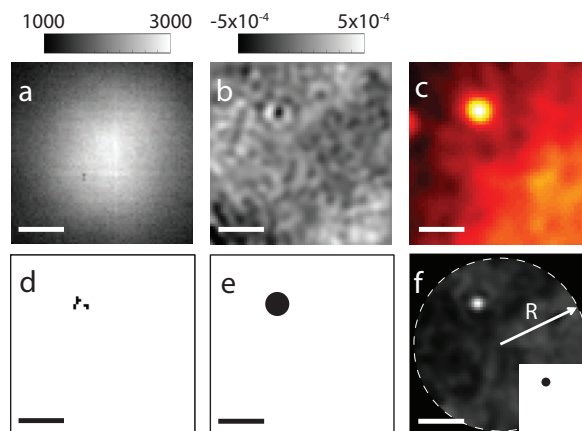


**Fig. 2.** Benchmarking methods for BSA (66 kDa). **a**, RAW iSCAT camera image. **b**, Outcome of a standard differential rolling average (DRA) treatment. Footprint of one BSA protein is evident on a residual speckle-like background. **c**, Raw TIRF image for the same protein landing event as in **(a,b)**. **d**, Hot pixels resulting from a user-defined AD analysis. **e**, Binary mask generated from the event detected in **(d)**. **f**, Probability map of AD based on DNN. Parameter  $R$  indicates the radius of the central circular part of the image that was considered in the analysis. Inset shows the corresponding binary mask. Scale bars are  $1.5 \mu\text{m}$ .

### 110 **Pushing the detection limit**

111 Having established the principle of our new methodology, we now showcase its performance by measuring proteins that have  
 112 not been previously detectable. Figs. 3a-c displays examples of three TIRF images, which confirm the presence of proteins  
 113 with molecular mass of 21, 18, and 9 kDa, respectively. In Figs. 3d-f, we present the corresponding DRA-treated images. To  
 114 guide the eye, we placed crosses (x) at the locations of protein landing events as determined from the centers of the PSFs in  
 115 their corresponding TIRF images. Distinguishing the protein PSF from the speckle-like background appears not to be within  
 116 reach in any of the cases. Remarkably, however, the data in Figs. 3g-i show that AD based on user-defined features can identify  
 117 the protein landing events. The success of this procedure can be traced to the fact that our algorithm imposes simultaneous  
 118 temporal and spatial requirements to the located anomalous events (see SI, section 4).

119 Figs. 3j-l shows the probability maps of the events obtained from a DNN analysis, and Figs. 3m-o plots the corresponding  
 120 outcome of iForest classification. We note that we put a more stringent condition on the morphological operation at lower SNRs  
 121 and only included events with at least three connected pixels in each frame (see SI, Table 1). Both the user-defined and DNN  
 122 approaches succeed in detecting the protein event under study in the data presented in Fig. 3. However, the yield of the former  
 123 method decreases as the SNR is diminished. For the 9 kDa sample, the DNN yield is about four times higher.

124 To elucidate the advantage of DNN further, we synthetically lowered the SNR of the landing event discussed in Fig. 2 by  
 125 reducing the DRA window size. Figs. 4a and 4b depict the outcome of two DRA averaging window sizes of 750 and 250  
 126 frames, respectively. As depicted in Figs. 4c and 4d, the user-defined approach is not able to detect the protein for the smaller  
 127 averaging window whereas Figs. 4e and 4f show that DNN succeeds in both cases.

128 We have presented several cases where iSCAT detection of protein landing events was confirmed by TIRF images. However,  
 129 one has to bear in mind that the modulation of the iSCAT contrast in the speckle-like background may cause false positive  
 130 events or mask a true event. Similarly, landing events might be absent in the TIRF channel, e.g., due to photobleaching or  
 131 imperfect labelling. Consequently, the yield in obtaining a one-to-one correspondence between the TIRF and iSCAT data was  
 132 low. One example appears in the event presented for the detection of a 21 kDa protein in Fig. 3, where AD detects two proteins  
 133 while TIRF only provides a robust signature of one of them. Fig. 5a shows another example of several events captured in the  
 134 iSCAT (blue) and TIRF (red) channels recorded within 20 s. In Fig. 5b, we display the coincidence map of the two signals  
 135 obtained by constructing the pixel-wise product of the localized events.

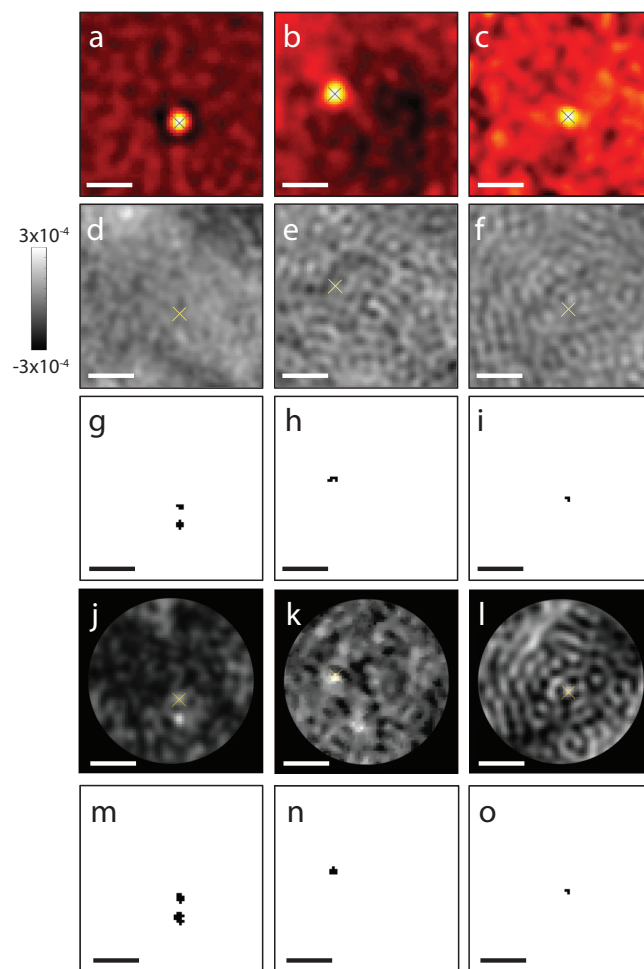


**Fig. 3.** Detection of very small proteins with molecular mass of 21 kDa (left column), 18 kDa (middle column), 9 kDa (right column) . **a-c**, TIRF images associated with the landing of 21 kDa (**a**) , 18 kDa (**b**) , and 9 kDa (**c**) proteins. **d-f**, Results of a standard DRA analysis. Crosses illustrate the centers of the landing events deduced from images in (**a-c**). **g-i**, Outcome of iForest classification for a user-defined AD. **j-l**, Probability maps obtained from a DNN analysis. **m-o**, Results of iForest classification based on probability maps in (**j-l**). Scale bars are set to 1.5  $\mu\text{m}$ .

### Protein mass photometry

Once the PSFs of individual particles have been localized by AD (user-defined or DNN), their iSCAT contrasts can be extracted as in previous reports<sup>14</sup> (see also SI, Fig. 3). The blue histograms in Figs. 5c-e display the distribution of the iSCAT contrasts obtained from 21, 18, and 9 kDa protein samples following the full DNN-based AD algorithm. In addition, the orange histograms in this figure present the spread of the contrasts obtained for the iSCAT events that coincided with an event detected in the TIRF channel. We find that although the yield is lower in the latter case, the main modes of the histograms are very well aligned. The Gaussian mixture model (GMM) was used to identify the underlying sub-populations and the mean of their contrast values in each histogram<sup>14,22</sup>. We note that the distribution towards higher contrasts can be attributed to small populations of oligomeric states of the protein, protein aggregates, or sample impurities<sup>12</sup>.

The deduced contrast can be related to mass if one assumes a common density and refractive index for proteins<sup>8,12,14</sup>. Because parameters  $r$  and  $s$  (see Eq. 1) can vary among individual iSCAT setups, one needs to establish a calibration ladder, much in the spirit of the read-out procedure in gel electrophoresis. Fig. 6a presents such a library, which contains the data from protein samples with nominal molecular mass of 220, 66, 21, 18, and 9 kDa as well as a linear fit.

In Fig. 6b, we plot the accuracy in units of kDa as the difference between the measured mean value and the value suggested by the fit. Fig. 6c presents the precision (in per cent) in determining the center of a Gaussian function that is fitted to the main mode of the histogram<sup>14</sup> analogous to the procedure in localization microscopy<sup>23</sup>. It is evident that both the accuracy and precision become less robust for the smallest protein size. We also point out a slight offset at the intercept of the linear fit on the vertical axis. We attribute this to the fact that the background fluctuations cannot be fully eliminated, thus, affecting the base

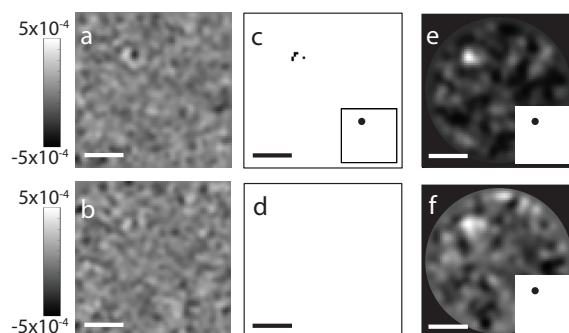


**Fig. 4.** User-defined vs DNN performance at different SNR. **a, b**, Outcome of DRA for averaging window sizes of 750 (**a**) and 250 (**b**) frames applied to the data presented in Fig. 2. **c, d**, Outcome of AD based on a user-defined feature bank for the DRA window sizes of 750 (**c**), and 250 (**d**). **e, f**, Probability maps based on DNN for the DRA window sizes of 750 (**e**), and 250 (**f**). Insets in (**c, e, f**) show the corresponding binary masks. Scale bars equate to  $1.5 \mu\text{m}$ .

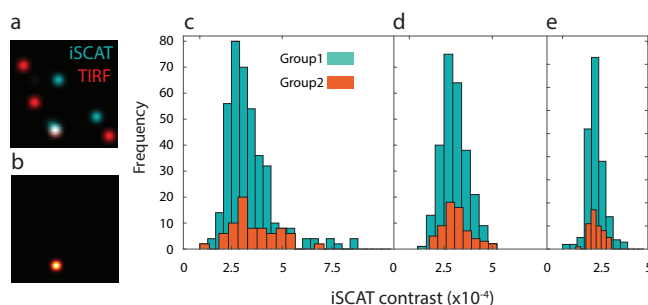


**Fig. 5.** **a**, Overlay of landing events for a protein sample at 21 kDa recorded on the TIRF (red) and iSCAT (blue) channels during a period of 20 s. **b**, Correlation map between the iSCAT and TIRF channels. **c-e**, Histograms of the binding events for the 21 kDa (**c**), 18 kDa (**d**), and 9 kDa (**e**), protein samples, respectively. Group 1 depicts the contrast value of the localized proteins resulting from DNN-based AD. Group 2 represents the binding events which appeared on both TIRF and iSCAT channels.

154 line for assessing a contrast<sup>14</sup>. Nevertheless, the linear model in Fig. 6a displays an RMS deviation of  $1.0 \times 10^{-5}$ , which is, to  
 155 the best of our knowledge, the lowest value reported for such protein libraries<sup>12,22</sup>.

## 156 Discussion and outlook

157 The first publications that demonstrated the ability of iSCAT for label-free detection of single proteins appeared in 2014  
 158 regarding the detection of 500 kDa (myosin 5a)<sup>24</sup> and 66 kDa (BSA)<sup>8</sup> proteins. Since then, the sensitivity limit has been  
 159 somewhat improved to 55 kDa<sup>12</sup> and about 40 kDa<sup>11</sup>, whereby the application of a spatial mask in the Fourier plane was  
 160 considered to be instrumental for favoring the scattered signal<sup>12,25,26</sup>. In our current work, we employ an anomaly detection  
 161 machine learning algorithm to substantially push the sensitivity limit to proteins as small as 9 kDa. Moreover, we achieve this  
 162 without using a spatial mask.

163 Although the yield of our new approach is lower than what is obtained for larger particles, we have verified that the  
 164 fidelity of the results is not compromised. Access to label-free and real-time analysis of small proteins is very promising for  
 165 ultrasensitive diagnostics of disease markers such as interleukins or other cytokines in bodily fluids<sup>27</sup>. Moreover, a range of  
 166 fundamental studies such as assembly of biological nanostructures<sup>28</sup>, cell secretion<sup>29,30</sup>, and protein aggregation studies which  
 167 are indicators of neurodegenerative diseases<sup>31</sup>.

168 Label-free detection of biomolecules can be further advanced through improvements in the physical measurements such as  
 169 CMOS technologies with larger full well capacity and lower dark noise, or the use of higher quality of the substrate surface for  
 170 lowering the iSCAT background. In addition, as machine learning approaches become more established in microscopy<sup>16,32-35</sup>,  
 171 one can also expect further advances in the computational analysis of label-free sensing. A first measure, e.g., could involve  
 172 replacing iForest with an end-to-end DNN. We note that the methodology presented in this work also holds promise for efforts  
 173 in cryogenic electron microscopy and fluorescence microscopy with low signal-to-noise ratio.

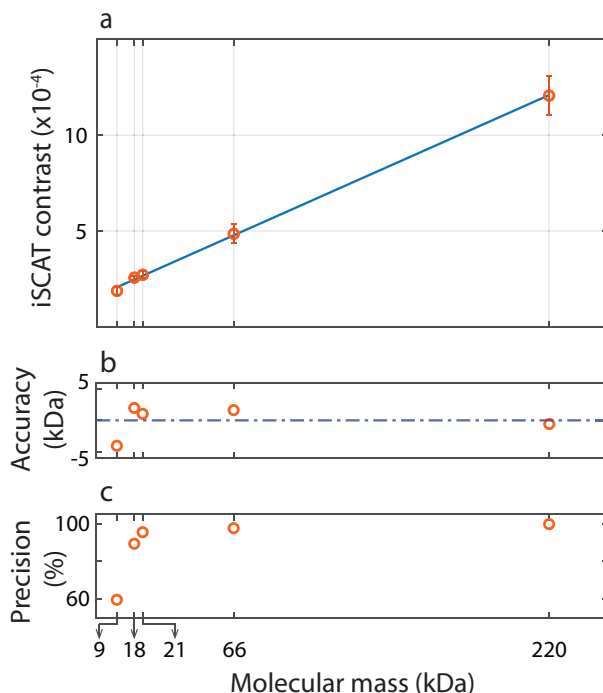


**Fig. 6. a**, Protein contrast library. Five different samples, ranging from 9 to 220 kDa were measured and compiled to form the library. The iSCAT contrast scales linearly with the nominal molecular mass of the protein sample. **b**, The distance of the points from the fitted linear model were calculated in terms of molecular mass to produce a measure for accuracy. The horizontal dashed line indicates zero. **c**, Error bars (expressed in percentage) associated with each data point in (a) depicting the uncertainty in assigning the main mode of the histograms and, thus, allocating an iSCAT contrast.

## 174 Methods

### 175 Protein sample preparation and labeling

176 All proteins used in this study are commercially available in a highly pure quality. Human plasma fibronectin (220KD) was  
 177 purchased from Sigma Aldrich (Cat: FC010). UltraPure Bovine Serum Albumine (BSA, 66 KD) was purchased from Life  
 178 Technologies GmbH (Cat: AM2616) Sigma). Recombinant protein G (21 KD) was purchased from Fisher Scientific (Cat:  
 179 15807617). Recombinant E. Coli Skp protein (18 KD) and Recombinant human IL-8 protein (9 KD) were purchased from  
 180 Abcam (Cat: ab97397 and ab9631 respectively). Proteins were diluted or buffer exchanged (desalted) into labeling buffer  
 181 which contain 50 mM HEPES, 25 mM KCl at pH 7.8, prior to the labeling reaction, using a 7K MWCO Zeba desalting  
 182 column (ThermoFischer, cat. 89882). Proteins were unspecifically labeled via their exposed primary amines using ATTO647  
 183 fluorophore containing the reactive group NHS Ester (catalogue number 18373-1MG-F, Sigma Aldrich). Proteins were mixed  
 184 with dyes at a ratio of 1:4 for 2 hr at room temperature, and then desalted from the excess of dye using the same desalting  
 185 columns. Proteins were further filtered using 100 nm syringe filter (Whatmann Anotop 10, Cat: WHA68091002, Sigma  
 186 Aldrich). The labeling efficiency was then estimated using an absorption spectrometer (Nanodrop 2000, ThermoFischer).  
 187 SDS-page was finally used to assess protein purity, labeling and its rough molecular weight (Fig. 2, SI).

### 188 Coverglass functionalization

189 In order to functionalize the surface of the coverglass for protein binding, it was sonicated in isopropyl alcohol and ethanol for  
 190 5 minutes each, followed by 10 minutes of oxygen plasma. The sample was then mounted and left to stabilize for a few hours.

### 191 Protein injection and data acquisition

192 Each labeled protein sample was diluted down to about 10 nM in concentration, and 10  $\mu$ l of it was manually injected by  
 193 micropipetting on top of the iSCAT field of view. This is then immediately followed by starting the iSCAT camera data  
 194 acquisition which triggers the blue iSCAT laser. After about 20 s of data acquisition, the blue laser is switched off and the  
 195 red laser (TIRF channel) is switched on for 10 s. This is then followed by several cycles of interlaced iSCAT and TIRF data  
 196 acquisition, to reach a satisfactory data volume for meaningful statistics. Depending on the protein size, the iSCAT camera was  
 197 set to run at 5 to 15 kHz at an exposure time of 20  $\mu$ s.

## 198 **Optical setup**

199 A CW laser centred at  $\lambda = 445$  nm (iBeam smart, Toptica) is collimated and focused onto the back focal plane of an oil-  
200 immersion microscope objective ( $\alpha$  Plan-Apochromat 100x/1.46, Zeiss). A coverglass is positioned at the focus of the  
201 microscope objective using a piezo positioner (Nano-LPQ, Mad City Labs). The iSCAT field is imaged by a scientific CMOS  
202 camera (MV1-D1024E-160-CL, Photonfocus).

## 203 **Author contributions statement**

204 M.D. built the iSCAT setup and conducted all measurements. H.M. prepared and labeled the protein samples. M.D. and H.M.  
205 augmented the fluorescence measurement. H.M.D. constructed the analysis pipeline. M.D. and H.M.D. analyzed the data. H.K.  
206 and V.S. supervised the project. V.S., M.D., and H.M.D. wrote the paper.

## 207 **1 Data Availability**

208 The scripts reported in this paper have been deposited at PiSCAT<sup>36</sup>: <https://github.com/SandoghdarLab/PiSCAT>.  
209 The data is available upon reasonable request.

## References

- 210 **1.** Hong, M., Zhang, Y. & Hu, F. Membrane protein structure and dynamics from NMR spectroscopy. *Annu. Rev. Phys. Chem.* **63**, 1–24 (2012).
- 211 **2.** Zhu, Z., Lu, J. J. & Liu, S. Protein separation by capillary gel electrophoresis: a review. *Anal. Chim. Acta* **709**, 21–31
- 212 (2012).
- 213 **3.** Bai, X.-C., McMullan, G. & Scheres, S. H. How Cryo-EM is revolutionizing structural biology. *Trends Biochem. Sci.* **40**,
- 214 (2015).
- 215 **4.** Sauer, M. & Heilemann, M. Single-molecule localization microscopy in eukaryotes. *Chem. Rev.* **117**, 7478–7509 (2017).
- 216 **5.** Kaushik, A. Advances in Nanosensors for Biological and Environmental Analysis: Book Review. *Biosensors* **9**, 101,
- 217 [10.3390/bios9030101](https://doi.org/10.3390/bios9030101) (2019).
- 218 **6.** Sandoghdar, V. Nano-Optics in 2020  $\pm$  20. *Nano Lett.* **20**, 4721–4723, [10.1021/acs.nanolett.0c02199](https://doi.org/10.1021/acs.nanolett.0c02199) (2020).
- 219 **7.** Kukura, P., Celebrano, M., Renn, A. & Sandoghdar, V. Single-Molecule Sensitivity in Optical Absorption at Room
- 220 Temperature. *J. Phys. Chem. Lett.* **1**, 3323–3327, [10.1021/jz101426x](https://doi.org/10.1021/jz101426x) (2010).
- 221 **8.** Piliarik, M. & Sandoghdar, V. Direct optical sensing of single unlabelled proteins and super-resolution imaging of their
- 222 binding sites. *Nat. Commun.* **5**, 4495 (2014).
- 223 **9.** Lindfors, K., Kalkbrenner, T., Stoller, P. & Sandoghdar, V. Detection and Spectroscopy of Gold Nanoparticles Using
- 224 Supercontinuum White Light Confocal Microscopy. *Phys. Rev. Lett.* **93**, 037401 (2004).
- 225 **10.** Taylor, R. W. & Sandoghdar, V. Interferometric scattering microscopy: seeing single nanoparticles and molecules via
- 226 Rayleigh scattering. *Nano Lett.* **19**, 4827–4835 (2019).
- 227 **11.** Priest, L., Peters, J. S. & Kukura, P. Scattering-based Light Microscopy: From Metal Nanoparticles to Single Proteins.
- 228 *Chem. Rev.* **121**, 11937–11970 (2021).
- 229 **12.** Young, G. *et al.* Quantitative mass imaging of single biological macromolecules. *Science* **360**, 423–427 (2018).
- 230 **13.** Taylor, R. W. & Sandoghdar, V. *Interferometric Scattering (iSCAT) Microscopy and Related Techniques*, chap. 2, 25–65
- 231 (Springer International Publishing, 2019).
- 232 **14.** Dastjerdi, H. M. *et al.* Optimized analysis for sensitive detection and analysis of single proteins via interferometric
- 233 scattering microscopy. *J. Phys. D.* **55**, 054002 (2021).
- 234 **15.** Pang, G., Shen, C., Cao, L. & Hengel, A. V. D. Deep learning for anomaly detection: A review. *ACM Comput. Surv.* **54**,
- 235 1–38 (2021).
- 236 **16.** Möckl, L., Roy, A. R., Petrov, P. N. & Moerner, W. E. Accurate and rapid background estimation in single-molecule
- 237 localization microscopy using the deep neural network BGnet. *PNAS* **117**, 60–67 (2019).
- 238 **17.** Ting, K., Liu, F. & Zhou, Z. Isolation forest. In *IEEE International Conference on Data Mining, ICDM 2008*, 413–422
- 239 (IEEE, 2008).
- 240 **18.** Midtvedt, B. *et al.* Quantitative digital microscopy with deep learning. *Appl. Phys. Rev.* **8**, 011310 (2021).
- 241 **19.** Xu, Y., Wu, T., Gao, F., Charlton, J. R. & Bennett, K. M. Improved small blob detection in 3D images using jointly
- 242 constrained deep learning and Hessian analysis. *Sci. Rep.* **10**, 1–12 (2020).
- 243 **20.** Chandola, V., Banerjee, A. & Kumar, V. Anomaly detection: A survey. *ACM Comput. Surv.* **41**, 1–58 (2009).
- 244 **21.** Tassano, M., Delon, J. & Veit, T. Fastdvdnet: Towards real-time deep video denoising without flow estimation. In
- 245 *Proceedings of CVPR*, 1354–1363 (2020).
- 246 **22.** Sonn-Segev, A. *et al.* Quantifying the heterogeneity of macromolecular machines by mass photometry. *Nat. Commun.* **11**,
- 247 1–10 (2020).
- 248 **23.** K.I. Mortensen, J. S., L.S. Churchman & Flyvbjerg, H. Optimized localization analysis for singlemolecule tracking and
- 249 super-resolution microscopy. *Nat. Methods* **7**, 377–381 (2010).
- 250 **24.** Ortega Arroyo, J. *et al.* Label-Free, All-Optical Detection, Imaging, and Tracking of a Single Protein. *Nano Lett.* **14**,
- 251 2065–2070 (2014).
- 252 **25.** Cole, D., Young, G., Weigel, A., Sebesta, A. & Kukura, P. Label-free single-molecule imaging with numerical-aperture-
- 253 shaped interferometric scattering microscopy. *ACS Photonics* **4**, 211–216 (2017).
- 254
- 255

- 256 **26.** Liebel, M., Hugall, J. T. & van Hulst, N. F. Ultrasensitive label-free nanosensing and high-speed tracking of single proteins.  
257 *Nano Lett.* **17**, 1277–1281 (2017).
- 258 **27.** Seruga, B., Zhang, H., Bernstein, L. J. & Tannock, I. F. Cytokines and their relationship to the symptoms and outcome of  
259 cancer. *Nat. Rev. Cancer.* **8**, 887–899 (2008).
- 260 **28.** Garmann, R. F., Goldfain, A. M. & Manoharan, V. N. Measurements of the self-assembly kinetics of individual viral  
261 capsids around their RNA genome. *PNAS* **116**, 22485–22490 (2019).
- 262 **29.** Zhang, M. & Schekman, R. Unconventional Secretion, Unconventional Solutions. *Science* **340**, 559–561 (2013).
- 263 **30.** McDonald, M. P. *et al.* Visualizing Single-Cell Secretion Dynamics with Single-Protein Sensitivity. *Nano Lett.* **18**,  
264 513–519 (2018).
- 265 **31.** Ross, C. A. & Poirier, M. A. Protein aggregation and neurodegenerative disease. *Nat. Med.* **10**, S10–S17 (2004).
- 266 **32.** Li, Y., Xue, Y. & Tian, L. Deep speckle correlation: a deep learning approach toward scalable imaging through scattering  
267 media. *Optica* **5**, 1181 (2018).
- 268 **33.** Wang, F., Henninen, T. R., Keller, D. & Erni, R. Noise2atom: unsupervised denoising for scanning transmission electron  
269 microscopy images. *Appl. Microsc* **50**, 23 (2020).
- 270 **34.** Sheth, D. Y. *et al.* Unsupervised deep video denoising. In *ICCV*, 1759–1768 (2021).
- 271 **35.** Speiser, A. *et al.* Deep learning enables fast and dense single-molecule localization with high accuracy. *Nat. Methods* **18**,  
272 1082–1090 (2021).
- 273 **36.** Dastjerdi, H. M., Mahmoodabadi, R. G., Bär, M., Sandoghdar, V. & Köstler, H. PiSCAT: A Python Package for  
274 Interferometric Scattering Microscopy. *J. Open Source Softw.* **7**, 4024 (2022).

## 275 **2 Acknowledgements**

276 We thank Alexey Shkarin for help with the iSCAT camera acquisition software (pyLabLib Cam-control), Maksim Schwab for  
277 the mechanical components and Tobias Utikal for technical support. We would also like to thank Franz Wieser, Hengameh  
278 Mirzaalian, Martin Blessing, Kiarash Kasaian and Katharina König for providing valuable comments on our manuscript. V.S.  
279 and H.MD. acknowledge fruitful discussions with Reza Gholami Mahmoodabadi. This work was supported by the Max Planck  
280 Society.

## 281 **Competing interests**

282 The authors have no conflict of interest.

## Supplementary Files

This is a list of supplementary files associated with this preprint. Click to download.

- [SI.pdf](#)
- [NMETHA49307Teditorialpolicyflat.pdf](#)